A Compact DC–200 MHz Hybrid Current Measurement Approach for Fast Switching Power Semiconductor Modules

Shiqi Ji, *Senior Member, IEEE*, Wenhao Xie, *Student Member, IEEE*, Yikang Xiao, *Student Member, IEEE*, Ran Lu, Zhengming Zhao, *Fellow, IEEE*, Chao Sheng, and Weitao Yang

***Abstract*—The accurate current measurement is critical for power semiconductor characterization. Considering the switching speed of power semiconductors has become much faster in recent years, it is difficult to measure the current effectively using existing current probes due to their limited bandwidth. Also, in many cases, it is necessary to directly characterize power semiconductors in real power converters in long-term operations, requiring some other key specifications on current probes including dc accuracy, galvanic isolation, easy installation, etc. This article proposes a novel hybrid current measurement method, including the tunnel-magnetoresistance-based low frequency measurement section, Rogowski coil-based high-frequency measurement section, and signal conditioning circuits for seamless frequency combination. Accordingly, a current probe based on the proposed method is developed, achieving high bandwidth, galvanic isolation, and compact size. The performance is experimentally validated with a double pulse test and long-term continuous pulse test in a 1.2 kV/120 A SiC MOSFET power module-based converter platform. Eventually, the proposed probe is comprehensively compared with the commercial shunt and Rogowski coil.**

***Index Terms*—Current measurement, high bandwidth, Rogowski coil, tunnel magnetoresistance (TMR).**

I. Introduction

THE power semiconductor characterization plays a key role in the power conversion system design, including static output characterization [1], switching transient characterization [2], reliability test [3], etc. Among them, the accurate measurement of power semiconductor's current is important and challenging, especially considering some upcoming demands including 1) rapid current measurement for wide band-gap (WBG) power semiconductors, which have much faster switching speed than Si counterparts [4]; and 2) convenient current measurement for power devices in real power converters both during periods of switching transients and long-term operations [5].

Considering these demands, the power semiconductor current measurement approach should meet following requirements.

1) High bandwidth. First, the WBG device current changes rapidly during switching transients. The fall time and rise time of the current could reach 10 ns level [6], requiring better high-frequency (HF) response [7]. Meanwhile, because that current needs to be measured both during switching transients and long-term operation, the dc performance of the current measurement should also be guaranteed [8], [9], [10].
2) Galvanic isolation and noise immunity capability. Due to higher *dv*/*dt* induced by WBG devices [11] as well as more complex electromagnetic interference in real power converters [12], the noise immunity capability is critical. The galvanic isolation enhances the safety and noise immunity of the measurement especially in power tests.
3) Compact size. In order for high power density, the power converter is often compactly designed [13]. The size for power semiconductor current measurement is even more limited. The current measurement equipment should be easily installed with compact size.

Some efforts have been made for the power semiconductor current measurement. The shunt resistor, which is essentially a low inductance resistor, has been widely used for the current measurement. Generally, the shunt has the highest bandwidth among all measurement methods. T&M research products can already provide shunts with bandwidth up to 2 GHz [14]. The HF design of the shunt with parasitic inductance reduction is discussed in [15]. But the shunt has to be inserted into the power stage, impacting the stray inductance as well as the galvanic isolation of the test. Meanwhile, considering the heat dissipation, the current range of the shunt is highly related to its power rating and size. In summary, the shunt is suitable for switching characterization in specially designed platforms, but not convenient for the current measurement in real power converters. The Rogowski coil also shows good performance in HF current measurement, as well as has benefits of noninsertion measurement, compact size, galvanic isolation, etc. PEM

Received 20 July 2024; revised 28 August 2024; accepted 20 September 2024. Date of publication 24 September 2024; date of current version 12 December 2024. This work was supported by the Program of the National Natural Science Foundation of China under Grant 52277189. Recommended for publication by Associate Editor H. S. Krishnamoorthy. *(Corresponding author: Shiqi Ji.)*

Shiqi Ji, Wenhao Xie, Yikang Xiao, Ran Lu, and Zhengming Zhao are with the Department of Electrical Engineering, Tsinghua University, Beijing 100084, China (e-mail: chic2020@tsinghua.edu.cn; xwh21@mails.tsinghua.edu.cn; xiaoyk16@tsinghua.org.cn; lur21@mails.tsinghua.edu.cn; zhaozm@tsinghua.edu.cn).

Chao Sheng and Weitao Yang are with the China Southern Power Grid Technology Company, Ltd., Guangzhou 510000, China (e-mail: shengchao@139.com; yangweitao188@163.com).

Color versions of one or more figures in this article are available at https://doi.org/10.1109/TPEL.2024.3467066.

Digital Object Identifier 10.1109/TPEL.2024.3467066

provided the Rogowski coil-based current probe with 1 Hz–50 MHz bandwidth [16]. The height of the Rogowski coil is only several millimeters. However, the accuracy of the Rogowski coil in the low frequency (LF) and dc range cannot be maintained. The HF bandwidth is also insufficient for the Rogowski with a flexible plastic skeleton coil. The PCB-based Rogowski coil has been introduced in [17] to improve the HF response. The current transformer (CT) is used for the ac measurement, especially made for current sensors [18]. Because the CT has a magnetic material-based coil, which is different from the air coil in the Rogowski, the bandwidth of CT is commonly limited [19]. But the HF CT with bandwidth up to tens of megahertz has also been published for partial discharge tests [20]. Hall effect is an important method for current sensors that have bandwidth from dc to hundreds of kilohertz [21]. Tektronix provided the HF Hall effect-based current probe with dc–50 MHz bandwidth [22], but without technical details published. But it is still rare to use the Hall effect in HF current measurement due to the relaxation time of carriers, inductive and capacitive effects, etc. [23]. The size of the Hall effect-based probe is generally large due to the complex structure of the Hall generator [24]. Recently, the tunnel magnetoresistance (TMR) has been widely used for the current measurement due to its high sensitivity, low power consumption, low temperature drift, etc. [25], [26], [27] By detecting the change of TMR resistance under variable static and dynamic magnetic field density, the current inducing the magnetic field can be obtained. Both ac and dc can be measured using the TMR. The TMR integrated circuit (IC) has already been commercialized with the integration of sensors and signal conditioning circuits in a chip. But the bandwidth of the TMR is still limited, only reaching several megahertz [28]. There have been other current measurement methods with compact size. The fluxgate magnetometer, which is used for magnetic field measurement, can be used for current measurement. The fluxgate magnetometer-based current probe with dc–5 MHz bandwidth has already been provided by Aim-TTi, measuring the PCB trace current conveniently [29]. However, considering the measurement result is very sensitive to the position of the probe, it is only suitable for rough current measurement. The optical-based current probe has been proposed with a very small sensor head and up to 150 MHz bandwidth in recent years [30]. However, the cost is very high due to material requirement and the performance has not been fully validated. The key performance comparison of different current measurement methods is listed in Table I.

TABLE I
KEY PERFORMANCE OF EXISTING CURRENT MEASUREMENT METHODS

Solution	Bandwidth	Size	Galvanic isolation
Shunt [14]	DC-2 GHz	Large	No
Rogowski coil [16]	1Hz-50 MHz	Small	Yes
Current transformer [20]	1Hz-10 MHz	Large	Yes
Hall effect current probe [22]	DC-50 MHz	Large	Yes
Tunnel magnetoresistance [28]	DC-5 MHz	Small	Yes
Fluxgate magnetometer [29]	DC-5 MHz	Small	Yes
Optical probe [30]	DC-150 MHz	Small	Yes
Hall sensor + transformer in [33]	DC-50 MHz	Large	Yes
Hall sensor + transformer in [34]	DC-30 MHz (not tested)	Large	Yes
Hall sensor + Rogowski in [35]	DC-50 MHz	Large	Yes
Hall sensor + Rogowski in [36]	DC-75 MHz	Large	Yes
Hall sensor + Rogowski in [37]	DC-3 MHz	Small	Yes
TMR + Rogowski in [38]	DC-10 MHz (not tested)	Small	Yes
TMR + Rogowski in [40]	DC-50 MHz (not tested)	Small	Yes
TMR + Rogowski in [41]	DC-380 MHz (not tested)	Small	Yes

*not tested means the bandwidth testing result in frequency-domain is not given

Considering it is difficult to accurately measure the power device current with a single approach, there have been ideas to combine different kinds of current measurement methods [31]. Qi et al. [32] proposed a combined solution with an HF ac probe for the commutation loop and data processing using the HF current and LF load current. The hybrid current measurement methods with the Hall effect for LF and transformer for HF have been proposed in [33], [34], and [35] to achieve better frequency response compared to conventional Hall effect-based current sensors. DC–300 kHz is achieved in [33] and highly improved to tens of megahertz in [34] and [35]. Considering the big size and HF limitation of the CT, the hybrid current measurement methods with Hall sensor for LF and Rogowski coil for HF have been proposed in [36] and [37] achieving a bandwidth of dc–75 MHz and smaller size compared to the CT. The methods have also been integrated into ICs for small current measurements [38]. However, due to a large size of the Hall sensor, these methods are commonly used as the load current measurement with frequency extension compared to existing current sensors. The hybrid methods with TMR for LF and Rogowski coil for HF are proposed recently achieving a more compact size [39], [40], [41], [42]. Nibir et al. [39] proposed a combined current measurement with TMR and Rogowski coil, achieving no invasion current test and a bandwidth of dc–10 MHz. But there is seemingly only one TMR IC used for LF measurement [40] and the accuracy under nonideal scenarios such as the targeted current has eccentric distance and inclination angle should be further studied. The circular TMR IC scheme is proposed in [41] to avoid the external magnetic field influence. Ziegler et al. [42] proposed an approach to overcome the limited operating region issue of the magnetic sensors by titling the TMR. But the size of the sensor head is inevitably larger, impacting the measurement for power modules. An HF bandwidth of dc–380 MHz is also claimed in [42]. But the effort to achieve the high bandwidth is not provided and the validation of the bandwidth with frequency-domain measurement results is not given in the article. Meanwhile, a 10% error is observed in experimental results and the cause is unclear.

The hybrid current measurement with TMR for LF and Rogowski for HF provided potential benefits in high bandwidth, galvanic isolation, and compact size. But it still suffers from accuracy and bandwidth issues, especially considering the nonideal characteristics including sensor heads, signal conditioning circuits, external magnetic field, environment, etc. The design considerations and methods should be studied in detail with these nonideal scenarios. Meanwhile, a more comprehensive validation, including frequency-domain and time-domain with performance during the switching transient and long-term operation, is necessary for this method.

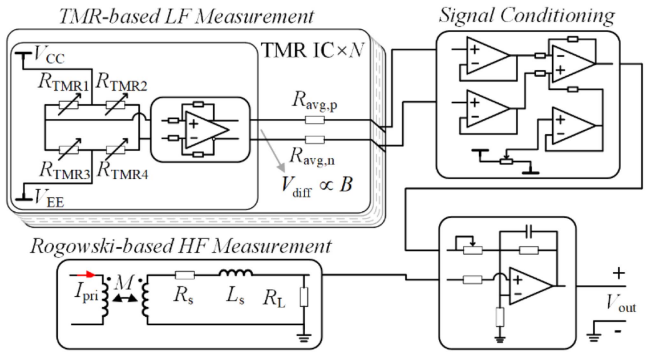

Fig. 1. Schematic of the proposed hybrid current measurement method.

The schematic of the proposed hybrid current measurement method, which can both measure the switching transient current and the LF component of power semiconductors with a bandwidth from dc to 200 MHz, is shown in Fig. 1. The LF section is measured with TMR and the HF section is measured with Rogowski coil. The signal conditioning circuit is designed to achieve the seamless combination of the LF and HF sections. The proposed method can measure the current from dc to hundreds of megahertz and achieve compact size and galvanic isolation as well.

The rest of the article is organized as follows. The design consideration of the TMR-based LF measurement section is presented in Section II. The Rogowski coil-based HF measurement section is introduced in Section III. The signal conditioning circuit in order for seamless combination of LF and HF sections is discussed in Section IV. A current probe based on the proposed method is implemented in Section V with comprehensive experimental validation and comparison with commercial products. Finally, Section VI concludes this article.

II. TMR-Based LF Measurement

With the commercialization of TMR IC in recent years, the TMR has become more and more popular in the measurement of the LF magnetic field from dc to several megahertz with high sensitivity and small size, eventually reflecting the targeted current which induces the magnetic field. Here, the TMR sensor is used for LF current measurement. It is important to arrange the location and number of TMR ICs properly.

N pieces of TMR ICs are placed as shown in Fig. 2(a), circulating the targeted current $I_{\rm pri}$. The TMR IC used in this article is composed of four tunnel effect-based magneto resistors, forming a Wheatstone Bridge. Within the saturation region of the magneto resistors, the output voltage of the TMR IC has a linear relationship with the magnetic field in the sensitive direction, which is placed as the orthogonal direction of $I_{\rm pri}$. Therefore, the output voltage of TMR IC reflects the magnetic flux $\Phi_{\rm m}$ within the IC area as shown in Fig. 2(a).

Defining the mutual inductance M as the ratio between $I_{\rm pri}$ and $\Phi_{\rm m}$. In the ideal case that $I_{\rm pri}$ is in the center of the circle and absolutely orthogonal with $\Phi_{\rm m}$, all TMR ICs have the same

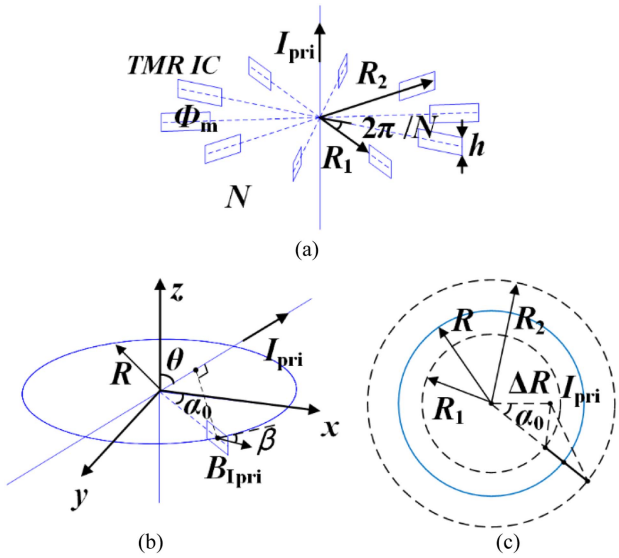

Fig. 2. TMR-based LF current measurement. (a) Schematics of TMR IC arrangement. (b) $I_{\rm pri}$ with inclination angle. (c) $I_{\rm pri}$ with eccentric distance.

output voltage, and M can be represented as

$$M(\alpha_0) = \frac{\mu_0 h}{2\pi} \ln\left(\frac{R_2}{R_1}\right) \tag{1}$$

where $\alpha_0 = (k\times 2\pi)/N$, $k = 1,2,\ldots N$, indicating the location of each TMR IC, R_1 and R_2 are inner and outer diameter, h is height of the TMR IC area. R_1, R_2, and h are 9, 10, and 1.5 mm, respectively.

Nonideal cases should be considered as well, including that $I_{\rm pri}$ has an angle of inclination shown in Fig. 2(b) and eccentric distance shown in Fig. 2(c). M can also be derived in these cases.

For $I_{\rm pri}$ with an inclination angle, M can be represented as

$$M(\alpha_0) = \frac{\mu_0 h}{2\pi} \ln\left(\frac{R_2}{R_1}\right) \times \frac{\cos\theta}{\sqrt{1-\sin^2\theta\sin^2\alpha_0}\sqrt{\cos^2\theta+\sin^2\theta\cos^2\alpha_0}} \tag{2}$$

while for $I_{\rm pri}$ with eccentric distance, M equals to

$$M(\alpha_0) = \frac{\mu_0 h}{4\pi} \ln\left(\frac{R_2^2+\Delta R^2-2R_2\Delta R\cos(\alpha_0)}{R_1^2+\Delta R^2-2R_1\Delta R\cos(\alpha_0)}\right) \tag{3}$$

where θ is the inclination angle and ΔR is the eccentric distance.

The average output voltage of overall TMR ICs is used as the outcome of the LF section. Therefore, the average value of M of all TMR ICs should be stable in all cases. A differential factor F is used as the judgement

$$F = \frac{|\sum M - NM_0|}{NM_0} \tag{4}$$

where M_0 is labeled as M in the ideal case (i.e., without eccentric distance and inclination angle), which can be calculated with (1).

A lower F indicates better performance of the LF section. The required N is simulated with various θ and ΔR, under $F = 0.1\%$ and 1%, respectively, as shown in Fig. 3. It should be noted that $\Delta R/R > 1$ means that $I_{\rm pri}$ is not within the circle of TMR

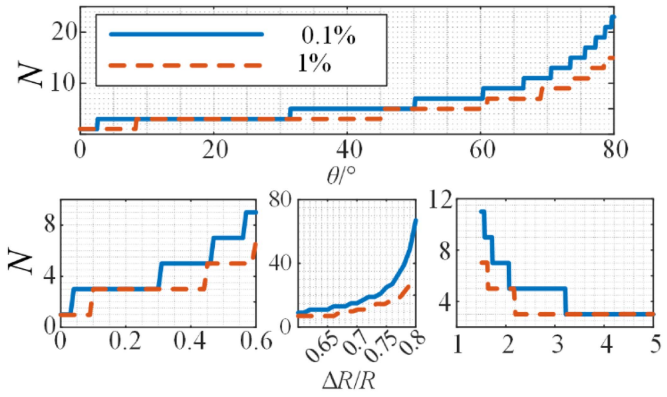

Fig. 3. Simulated results for relationship of $N-\theta$ and $N-\Delta R$.

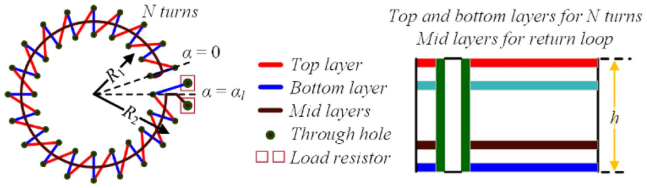

Fig. 4 Schematic diagram of the Rogowski coil.

ICs. In this case, F indicates that whether the impact of the current outside of the circle can be neglected. It can be seen that a larger N can obviously improve the accuracy, but increase the cost and size as well. Here, the current probe is designed for the measurement of the power semiconductor module with a relatively fixed location of $I_{\rm pri}$. Generally, θ is less than 60°, and $\Delta R/R$ is less than 0.5 or larger than 2. In order to achieve $F=0.1\%$, $N=8$ is selected here, meaning that 8 pieces of TMR ICs are placed.

III. Rogowski-Based HF Measurement

The Rogowski coil has been widely applied in the HF current measurement up to hundreds of megahertz. The mutual inductance between the Rogowski coil and the targeted current can be easily derived as

$$M = \frac{\mu_0 N h}{2\pi} \ln\left(\frac{R_2}{R_1}\right) \tag{5}$$

where R_1, R_2, and h are inner diameter, outer diameter, and height of the Rogowski coil, respectively, and N is the turn of the coil. R_1, R_2, h, and N are selected as 4.5 mm, 6.5 mm, 1.2 mm, and 19 turns. As shown in Fig. 4, the Rogowski coil is implemented in a four-layer PCB. The top layer and bottom layer are used for the layout of N turns whereas the mid layers are used for the return loop. In order for the HF response improvement, it is critical to understand the impact of parasitic parameters.

A. Derivation of Lumped Impedance

The equivalent circuit model of Rogowski coil considering the distributed parasitic parameters is given in Fig. 5. $C_{\rm tt0}$ and $C_{\rm tg0}$ are the equivalent serial and parallel parasitic capacitance

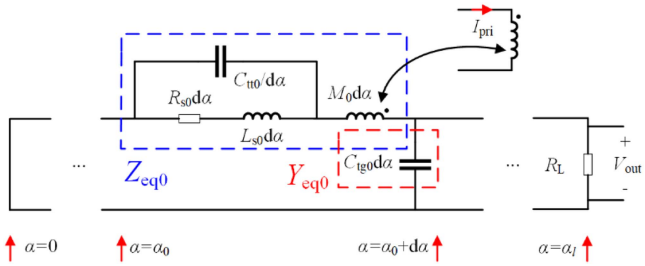

Fig. 5. Equivalent circuit model of Rogowski coil.

of each turn, respectively. $L_{\rm s0}$ and M_0 are the self inductance and mutual inductance of each turn, respectively. $R_{\rm s0}$ is the equivalent parasitic resistance and $R_{\rm L}$ is the load resistance, which is designed to match the output impedance of the Rogowski coil.

The transfer function of the Rogowski coil $Z_{\rm HF}$ can be derived similarly to that of the transmission line [43]

$$Z_{\rm HF} = \frac{V_{\rm out}}{I_{\rm pri}} = \frac{j\omega M_0 R_L}{\gamma\left(Z_0 + R_L \coth\left(\gamma\alpha_l\right)\right)} \tag{6}$$

where $Z_0 = \sqrt{Z_{\rm eq0}/Y_{\rm eq0}}$, and $\gamma = \sqrt{Z_{\rm eq0}Y_{\rm eq0}}$. $\alpha_{\rm l}$ represents the location of $R_{\rm L}$, as shown in Fig. 4. In the HF range, $|j\omega L_{s0}| \gg R_0$. Meanwhile, $C_{\rm tt0}$ is very low and can be neglected. Therefore, (6) can be derived as

$$Z_{\rm HF} \approx \frac{j\omega M R_L}{j\omega L_s + \omega\sqrt{L_s C_{tg}} R_L \cot\left(\omega\sqrt{L_s C_{tg}}\right)} \tag{7}$$

where $L_{\rm s}$ and $C_{\rm tg}$ are lumped self inductance and parallel parasitic capacitance of the Rogowski coil (i.e., $L_{\rm s}=\alpha_{\rm l}L_{\rm s0}$, $C_{\rm tg}=\alpha_{\rm l}C_{\rm tg0}$). $L_{\rm s}$ and $C_{\rm tg}$ can be obtained from Q3D simulation or measured with impedance analyzer. The HF response can be improved by reducing $C_{\rm tg}$. $C_{\rm tg}$ could be reduced to several pF, but it is difficult to totally eliminate the impact of $C_{\rm tg}$.

B. Impact of Load Resistance

The characteristics of $Z_{\rm HF}$ in (7) is determined by the ratio of the first item and second item of denominators. In the LF region (S1), where $\omega\sqrt{L_s C_{tg}} < \pi/4$, $\cot(\omega\sqrt{L_s C_{tg}}) \approx 1/(\omega\sqrt{L_s C_{tg}})$. Equation (7) can be derived as

$$Z_{\rm HF} \approx \frac{j\omega M R_L}{j\omega L_s + R_L}. \tag{8}$$

With increasing frequency (S2), where $\pi/4 < \omega\sqrt{L_s C_{tg}} < 3\pi/4$, $\cot(\omega\sqrt{L_s C_{tg}})$ changes from 1 to -1. If the second item of the denominator in (7) can be neglected, $Z_{\rm HF}$ is still relatively stable.

In HF range (S3), where $\omega\sqrt{L_s C_{tg}} \to \pi$, $\cot(\omega\sqrt{L_s C_{tg}}) \to -\infty$. $Z_{\rm HF}$ becomes zero and the Rogowski coil can not work in this region. Here, the resonant frequency of the Rogowski coil is defined as

$$f_{\rm res} = 1/\left(2\sqrt{L_s C_{tg}}\right) \tag{9}$$

the bandwidth of the coil can only be lower than $f_{\rm res}$.

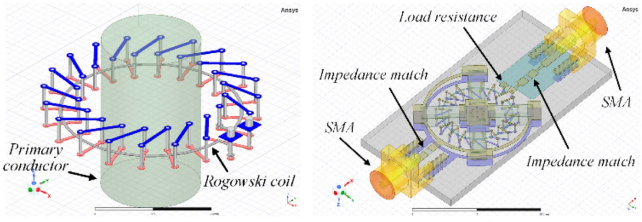

Fig. 6. Simulation configuration of Rogowski coil. (a) Key parameter simulation with Ansys Q3-D. (b) HF response simulation with Ansys HFSS.

TABLE II
SIMULATED AND EXPERIMENTAL RESULTS OF ROGOWSKI COIL

Parameters	Simulation	Experiment	Error
Self inductance L_s	97 nH	103 nH	-5.8%
Mutual inductance M	1.63 nH	1.65 nH	-1.2%
Parasitic capacitance C_{tg}	7.7 pF	7.2 pF	6.9%

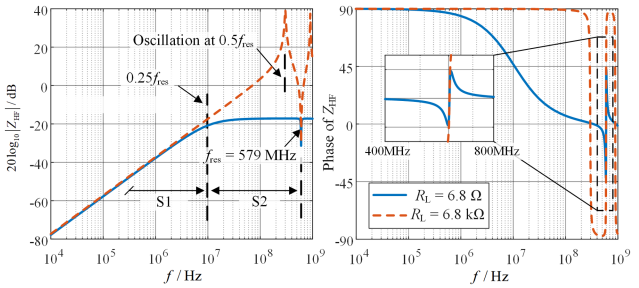

Fig. 7. HF response of Rogowski coil under various R_L.

The load resistance R_L plays a key role to maintain the HF response of the Rogowski coil. Three types of conditions are considered here.

1) When R_L is very high, in S2, the impact of the second item of the denominator in (7) becomes great. Z_{HF} changes severely in S2. Therefore, the Rogowski coil can only operate normally in S1 and the bandwidth is lower than $0.25f_{res}$.
2) When R_L is very low, in S1, Z_{HF} is already close to 0. The Rogowski coil can not work properly even in LF region.
3) The criteria to select the R_L is that $|j\omega L_s| < R_L$ in S1 but $|j\omega L_s| > R_L$ in S2. With a proper R_L, there is no significant change of Z_{HF} in S2 considering the second item can be ignored. The bandwidth could be higher than $0.25f_{res}$. A proper R_L is critical to improve the HF performance from $0.25f_{res}$ to $0.75f_{res}$.

The key parameters of the Rogowski coil are simulated with Ansys Q3-D model as shown in Fig. 6(a). L_s and C_{tg} are also experimentally characterized by a Vector Network Analyzer (VNA) Keysight E5061B. M can be obtained by the amplification factor of the HF measurement results. The simulated and experimental results are compared in Table II. The frequency-domain HF response of the Rogowski coil can also be simulated in Ansys HFSS with the model in Fig. 6(b). The simulated HF response with various R_L is given in Fig. 7. f_{res} is designed as 579 MHz. The HF responses of Rogowski coil with $R_L = 6.8$ kΩ and 6.8 Ω are compared. It can be seen that with a high $R_L = 6.8$ kΩ, there is an oscillation around $0.5f_{res}$, highly limiting the HF response in S2. With $R_L = 6.8$ Ω, the oscillation from $0.25f_{res}$ to $0.75f_{res}$ is obviously suppressed, which is helpful to improve the HF bandwidth of Rogowski coil.

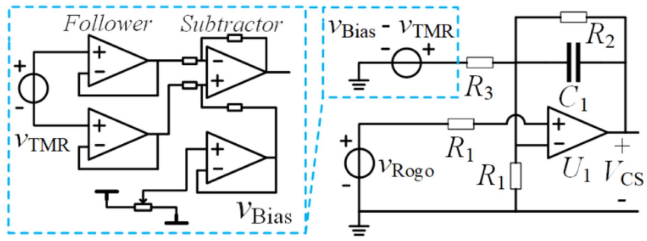

Fig. 8. Signal conditioning circuit of the proposed hybrid current measurement approach.

IV. SIGNAL CONDITIONING CIRCUIT

The signal conditioning circuit consists of two parts including: 1) signal conditioning for the TMR and Rogowski coil respectively based on their transfer functions; 2) signal conditioning for seamless combination of LF and HF sections.

The transfer function of TMR Z_{LF} and Rogowski coil Z_{HF} can be represented as

$$Z_{LF} \approx \frac{A_{0,LF}}{1 + j\omega T_{LF}} \tag{10}$$

$$Z_{HF} \approx \frac{MR_L}{L_s} \frac{j\omega T_{HF}}{1 + j\omega T_{HF}} \tag{11}$$

where $A_{0,LF}$ is the amplification factor of TMR IC and different for various model numbers. T_{LF} is the time factor of the TMR IC which is roughly 1 μs level. Here, the TMR is only used for the frequency range up to tens of kilohertz. T_{HF} is the time factor of the Rogowski coil and equals L_s/R_L.

The signal conditioning circuit is given in Fig. 8. The output of TMR IC v_{TMR} passes through a follower and subtractor by adding a bias voltage v_{Bias}. The output of the circuit is v_{Bias}-v_{TMR}. v_{Bias} is configured to ensure the output voltage equals zero when I_{pri} is 0. Afterward, the signal can be combined with the output of Rogowski coil v_{Rogo} using the circuit on the right side.

In order to match the impedance of the Rogowski coil Z_{HF}, R_1C_1 equals T_{HF} [15]. Considering R_1 is much lower than R_2 and R_3, the transfer functions of signal conditioning circuits of TMR H_{LF} and Rogowski coil H_{HF} can be described by

$$H_{LF} \approx \frac{R_2/R_3}{1 + j\omega T_{cor}} \tag{12}$$

$$H_{HF} \approx \frac{T_{cor}\,(1 + j\omega T_{HF})}{T_{HF}\,(1 + j\omega T_{cor})} \tag{13}$$

where $T_{cor} = R_2C_1$. The transition frequency between TMR and Rogowski coil $f_{cor} = 1/(2\pi T_{cor})$. The TMR will dominate the output below f_{cor} while the Rogowski coil will play a major role upper f_{cor}. Considering the limited bandwidth of TMR IC, f_{cor} can be selected as tens of kilohertz.

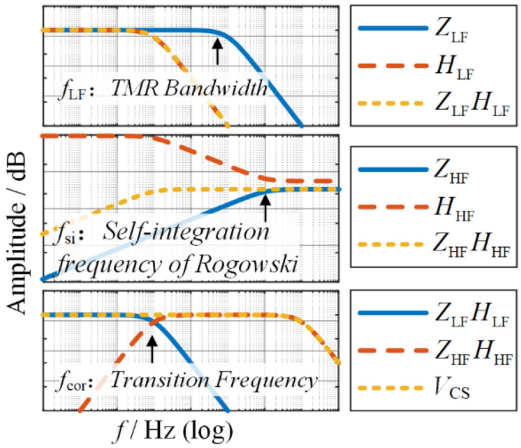

Fig. 9. Function of signal conditioning circuit.

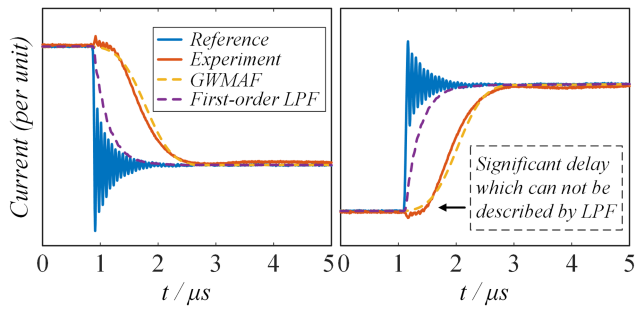

Fig. 10. Experimental and fitting results of TMR during switching transients.

The output voltage of TMR and Rogowski coil considering the signal conditioning circuit can be represented as

$$V_{\mathrm{LF}} = \frac{A_{0,\mathrm{LF}} R_2/R_3}{1 + j\omega T_{\mathrm{cor}}} I_{\mathrm{pri}} \tag{14}$$

$$V_{\mathrm{HF}} = \frac{MR_L}{L_s} \frac{j\omega T_{\mathrm{cor}}}{1 + j\omega T_{\mathrm{cor}}} I_{\mathrm{pri}}. \tag{15}$$

The seamless frequency transition can only be implemented when the amplification factors of TMR and Rogowski coil are the same, indicating $A_{0,\mathrm{LF}}R_2/R_3 = MR_{\mathrm{L}}/L_{\mathrm{s}}$.

With the combination of the outputs of the TMR and Rogowski coil, the overall output of hybrid current measurement V_{CS} can be described by

$$V_{\mathrm{CS}} = V_{\mathrm{LF}} + V_{\mathrm{HF}} = Z_{\mathrm{CS}} I_{\mathrm{pri}}. \tag{16}$$

The function of the signal conditioning circuit can be explained as shown in Fig. 9. The self-integration frequency of Rogowski coil f_{si} is equal to $R_{\mathrm{L}}/(2\pi L_{\mathrm{s}})$. The TMR bandwidth f_{LF} here is 650 kHz. The experimental results of the output of TMR IC during switching transients are shown in Fig. 10. The reference in Fig. 10 is the experimental waveforms with both LF and HF sections. The experimental results are the tested output of TMR IC. If the TMR is modeled as a first-order low pass filter (LPF) with a bandwidth of 650 kHz, it can be seen that even though the rise/fall time is similar with experimental results, but

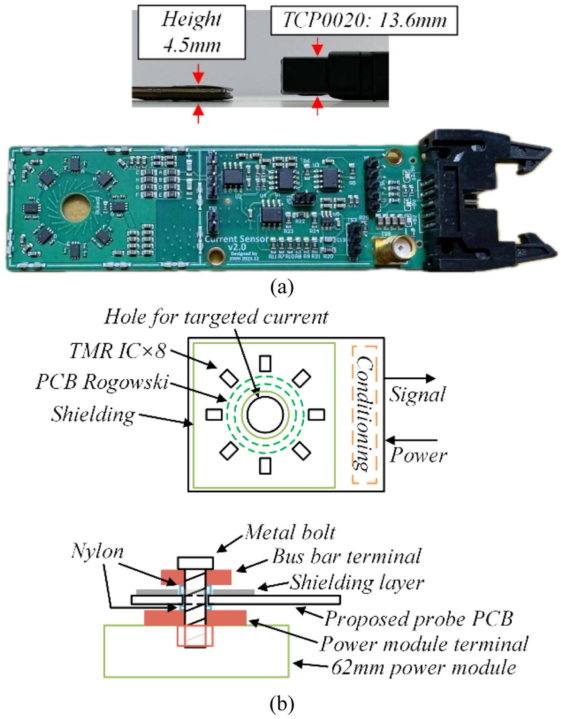

Fig. 11. Proposed current probe prototype. (a) Picture of prototype. (b) Schematic diagram of installation.

there is a significant delay, which is about hundreds of nanoseconds in experimental waveforms which cannot be described by the first-order LPF. Here, a Gause weighted moving average filter (GWMAF) is used to model the TMR, as represented as

$$y(t) = \frac{\int_{t-t_0}^{t} \exp\left\{-\frac{[p-(t-t_0/2)]^2}{2\sigma^2}\right\} x(p)\,\mathrm{dp}}{\int_{t-t_0}^{t} \exp\left\{-\frac{[p-(t-t_0/2)]^2}{2\sigma^2}\right\} \mathrm{dp}} \tag{17}$$

where t_0 and σ are selected as 1.8 μs and 0.36 μs respectively. It can be seen with the GWMAF, the fitting waveforms can match with the experimental results. Meanwhile, in order to avoid the impact of the delay from the TMR IC, the transition frequency f_{cor} is configured as 10 kHz by properly selecting R_2 and C_1.

V. Prototype and Experimental Validation

A dc–200 MHz current probe prototype with ±150 A range is developed as shown in Fig. 11. The height is only 4.5 mm, which is much thinner than Tektronix's commercial current probe TCP0020 with 20 Arms current range and dc-50 MHz bandwidth. The key parameters of the prototype are given in Table III. The current range is mainly determined by the amplification factor of TMR IC. The TMR IC used here has a *B-V* linearity region of ± 60 Gs. Considering the size of the sensor head, the magnetic field to current ratio can be calculated as 0.2 Gs/A. With consideration of the uneven distribution of magnetic field among all TMR ICs due to the impact of external conductors, a margin of 2 is used here to make sure all TMR ICs are within their linearity region. Therefore, the current range can be calculated as ±150 A. A higher current range can be

TABLE III
KEY PARAMETERS OF PROPOSED HYBRID CURRENT PROBE

Parameter	Value
Transition frequency f_{cor}	10 kHz
Self-integration frequency of Rogowski f_{si}	10.5 MHz
Resonant frequency of Rogowski f_{res}	579 MHz
TMR IC model number	TMR2652BD
Amplification factor of TMR IC $A_{0,LF}$	5 mV/A
Self inductance of Rogowski L_s	103 nH
Mutual inductance of Rogowski M	1.65 nH
Load resistance of Rogowski R_L	6.8 Ω
Size of the probe's measurement terminal	3 cm * 3 cm
Size of the probe with conditioning circuit	3 cm *10 cm

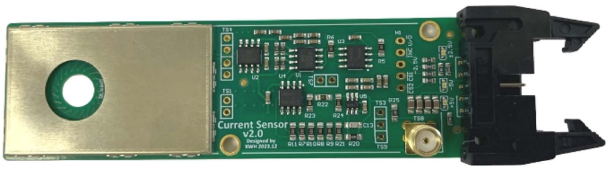

Fig. 12. Current measurement approach with shielding layer.

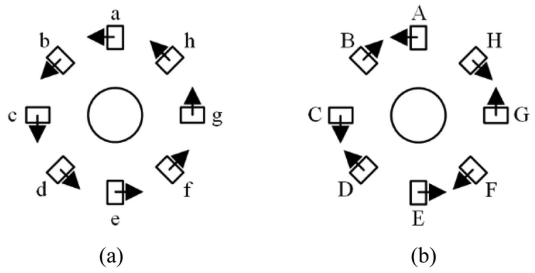

Fig. 13. Placement of TMR ICs. (a) Conventional placement. (b) Placement considering the temperature impact.

achieved by selecting a TMR IC model number with a larger linearity region and a lower mutual inductance for Rogowski coil, but the sensitivity will be reduced.

A. Implementation Considering Noise and Temperature

The high dv/dt during switching transients may cause interference issues for the measurement, especially the noise immunity for TMR IC is generally unknown. Two efforts have been done to improve the dv/dt immunity: 1) a shielding aluminum layer is placed as shown in Fig. 12 to isolate the dv/dt impact on the TMR IC and the Rogowski coil; 2) the proposed current probe is powered by a battery to avoid the common mode current induced by high dv/dt.

Considering the temperature change by hostile environment, etc., the temperature immunity design is important for the current measurement approach. There are four methods applied here to enhance the temperature immunity including the following.

1) Half of the TMR ICs are placed in a reverse direction as shown in Fig. 13. By this way, the voltage bias on the TMR ICs induced by the temperature change can be perfectly neutralized.

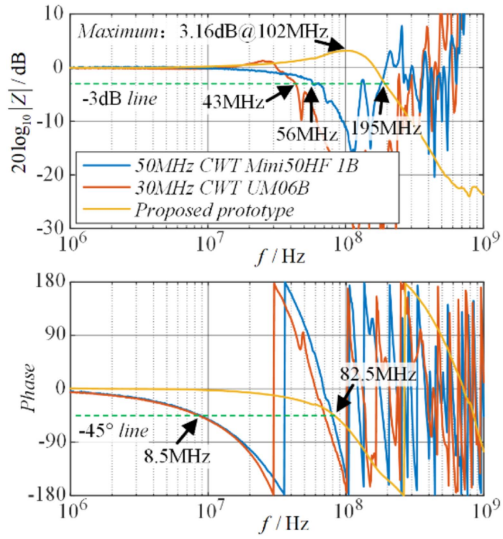

Fig. 14. HF bandwidth test using VNA for proposed current probe and commercial Rogowski coils.

2) Resistors with high resolution (0.1%) and low-temperature drift (100 ppm/°C) are applied for signal conditioning circuits.
3) A large area of copper ground layer and thermal conductive thermal pad are used to enhance the thermal dissipation capability of the current probe.
4) The input impedance of amplifier is matched to avoid the impact of the temperature drift current bias from the amplifier.

B. HF Bandwidth Test

The HF bandwidth is mainly determined by the bandwidth of Rogowski coil and its signal conditioning circuit. With R_L, the HF response of Rogowski coil can be improved from $0.25f_{res}$ to $0.75f_{res}$, and the bandwidth can be higher than $0.25f_{res}$ which is 145 MHz. The HF bandwidth can be measured by VNA Keysight E5061B. S1 of the VNA is used to supply a HF current with capability of less than 10 mA. S2 is connected with the output of the current probe. The HF bandwidths of the proposed current probe and commercial PEM's Rogowski coil are measured and compared in Fig. 14. The tested HF bandwidths of commercial CWT Mini50HF 1B and CWT UM06B are 56 MHz and 43 MHz, respectively, which are close to their bandwidths in datasheets (i.e., 50 MHz and 30 MHz). Considering the bandwidth limitation of the signal conditioning circuit, the overall HF bandwidth of the proposed current probe is approximately 200 MHz, which is better than the commercial Rogowski coils.

C. Switching Performance Test

A CREE's CAS120M12BM2 1.2 kV/120 A SiC MOSFET half-bridge power module with a typical 62 mm module package is used for the current measurement validation. The switching characteristics are tested in a multiple-pulse test platform. The testing results are compared with a commercial shunt T&M

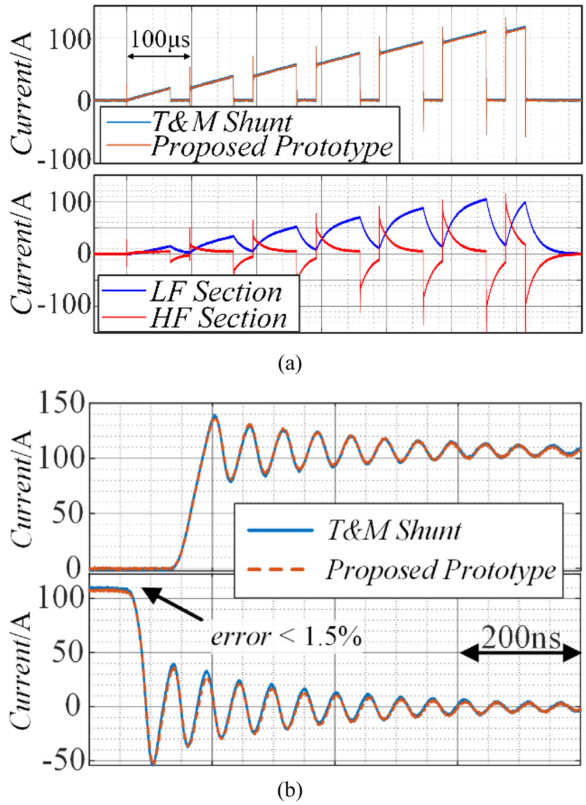

Fig. 15. Current measurement results of SiC MOSFET power module using proposed current probe and commercial shunt. (a) Overall waveforms of multiple pulse test. (b) Switching transient waveforms.

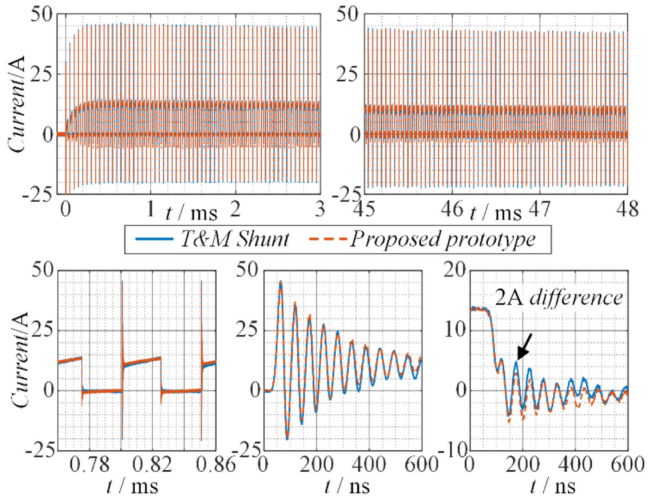

Fig. 16. Continuous current measurement of Buck converter using proposed current probe and commercial shunt with zoom-in single pulse waveforms and switching transient waveforms.

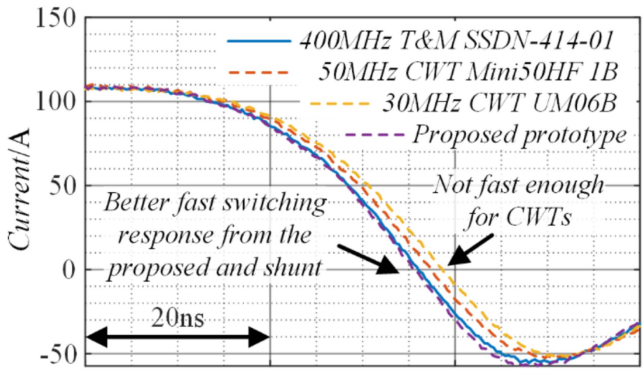

Fig. 17. Testing results comparison during the turn-off transient of SiC MOSFET using proposed current probe and commercial current probes.

SSDN-414-01 with dc-400 MHz bandwidth, as shown in Fig. 15. Fig. 15(a) shows the overall waveforms of the multiple pulse test, demonstrating the proposed prototype can provide good performance from LF to HF. The measurement output of LF and HF sections are also given in Fig. 15(a). The current waveforms during turn-ON and turn-OFF transients are given in Fig. 15(b). It can be seen that the testing results of the proposed current probe are nearly the same as that of the T&M shunt. The peak error is less than 1.5%, validating the accuracy of the proposed current probe for power semiconductor's fast switching characterization.

D. Continuous Pulse Test

The proposed current probe is also validated by a continuous pulse test in a Buck converter with 20 kHz switching frequency. Due to the output power limitation of the testing platform, the dc current rating is configured as 15 A and the peak current during switching transients is around 50 A. The testing results are compared with T&M SSDN-414-01. The testing waveforms from 0 to 3 ms and from 45 to 48 ms are given in Fig. 16 with zoom-in waveforms of switching transients and a single pulse. It can be seen that the testing results are nearly the same in long-term operation, validating the accuracy of the proposed current probe from dc to HF range as well as stability in the long-term operation. Therefore, the proposed current probe can be used for the multitime-scale current measurement of power converters, where both switching characterization and long-term performance testing are required. The current difference in testing results during switching transients is less than 2 A. It may be caused by common mode noise differences between the two types of approaches. A new common mode noise path will be provided by the shunt, but disappear if the proposed current probe is used due to the galvanic isolation.

E. Comparison With Commercial Current Probes

The proposed current probe is compared with two types of commercial current probes: 1) Rogowski coil CWT Mini50HF 1B with a bandwidth of 1 Hz-50 MHz and CWT UM06B with a bandwidth of 1 Hz-30 MHz; and 2) Shunt SSDN-414-01 with a bandwidth of dc–400 MHz.

The zoom-in current during the turn-OFF transient of SiC MOSFET power module is given in Fig. 17. The fall time of the current is 20 ns and peak *di/dt* reaches 10 A/ns. It can be seen that with 30 MHz and 50 MHz Rogowski coils, current speeds are lower than that using the proposed current probe and shunt. It means that the commercial Rogowski coils are not fast

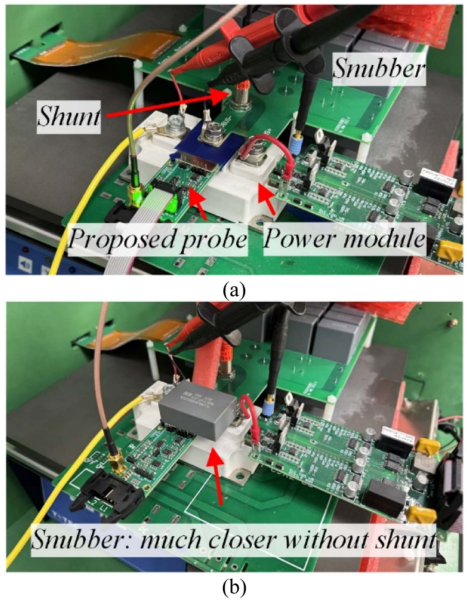

Fig. 18. Power stages of switching characteristics testing platform. (a) With shunt and proposed current probe. (b) Only with the proposed current probe.

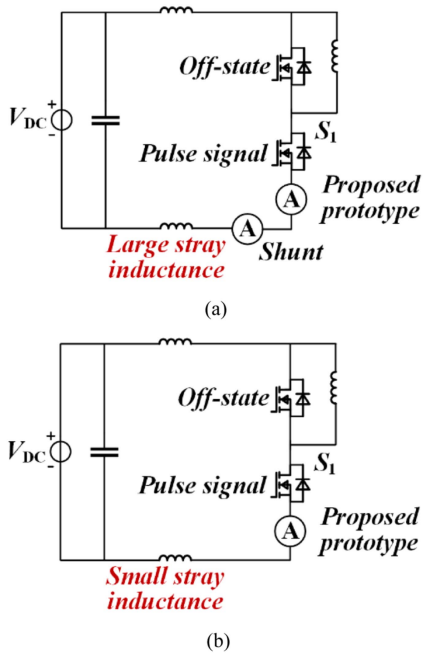

Fig. 19. Schematic diagrams of switching characteristics testing platform. (a) With shunt and proposed current probe. (b) Only with the proposed current probe.

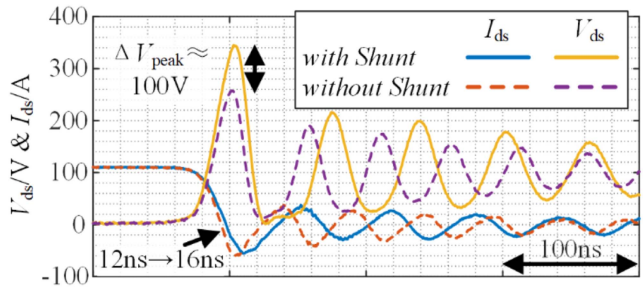

Fig. 20. Switching characteristic comparison with shunt and without shunt.

enough for current measurement during switching transients of SiC MOSFETs. Meanwhile, the testing results of the proposed current probe and the shunt are nearly the same, demonstrating a better accuracy for fast switching characterization.

Even though the shunt has higher bandwidth and better performance for fast switching transients, but the shunt has to be inserted into the power stage thus changing the commutation loop including the stray inductance, etc. The power stage with the proposed current probe and shunt are compared in Fig. 18, with the schematic diagram of the platforms given in Fig. 19.

Because the commutation loop becomes much longer with the shunt, the stray inductance is obviously higher even though using a laminated busbar design for the shunt. The switching characterization results with two kinds of power stages are given in Fig. 20. With the shunt in the power stage, the fall time of the current during the turn-OFF transient increases from 12 to 16 ns and the peak voltage increases from 250 to 350 V. The stray inductance has a significant impact on the switching characteristics of power modules, especially for fast-switching WBG devices. The proposed current probe is beneficial to measure switching characteristics in practical power converters without change on the power stage.

VI. Conclusion

A novel hybrid current measurement method is proposed and implemented in this article, including TMR-based LF measurement section, Rogowski coil-based HF measurement section, and signal conditioning circuit for seamless frequency combination. There are three major advantages of the proposed current measurement method, including: 1) high bandwidth from dc to 200 MHz; 2) compact size with a height of 4.5 mm; 3) galvanic isolation without common mode noise path and safety issue. Due to the advantages, the proposed current probe is beneficial to the characterization of fast-switching power semiconductors as well as power converters using these devices.

The accuracy and stability of the proposed current probe are experimentally validated with a double pulse test and continuous pulse test. The advantages of the proposed current probe are demonstrated by comparison with commercial probes including that: 1) compared to commercial Rogowski coils with 50 MHz bandwidth, the proposed current probe can achieve better HF performance due to its higher bandwidth; 2) compared to commercial shunts, the proposed current probe can be used for power semiconductor characterization in real power converters without change of the power stage.

Appendix

A. Derivation of Mutual Inductance for TMR and Rogowski

The magnetic flux density of a long straight conductor can be represented as

$$B = \frac{\mu_0 I_{\text{pri}}}{2\pi r}. \tag{A1}$$

The magnetic flux can be derived by integrating B in the desired area

$$\Phi_m = h\int_{R_1}^{R_2}\frac{\mu_0 I_{\text{pri}}}{2\pi r}dr = \frac{\mu_0 h I_{\text{pri}}}{2\pi}\ln\left(\frac{R_2}{R_1}\right). \tag{A2}$$

Defining the mutual inductance M as ratio between I_{pri} and Φ_{m}, M of a single turn can be represented as

$$M = \frac{\Phi_m}{I_{\text{pri}}} = \frac{\mu_0 h}{2\pi}\ln\left(\frac{R_2}{R_1}\right). \tag{A3}$$

For Rogowski coil with a large number of turns, the total M with N turns can easily be obtained

$$M = \frac{\mu_0 N h}{2\pi}\ln\left(\frac{R_2}{R_1}\right). \tag{A4}$$

If there is an inclination angle θ for I_{pri} as shown in Fig. 2(b), the distance between the turn and I_{pri} can be represented as

$$d = R\sqrt{1-\sin^2\theta\sin^2\alpha_0}. \tag{A5}$$

β is angle between the normal vector direction of the turn and the direction of B induced by I_{pri}, satisfying that

$$\cos\beta = \frac{1}{\sqrt{1+\tan^2\theta\cos^2\alpha_0}}. \tag{A6}$$

M can be derived as

$$M = \left[\frac{\mu_0 h}{2\pi}\ln\left(\frac{R_2}{R_1}\right)\right]\frac{R}{d}\cos\beta = \frac{\mu_0 h}{2\pi}\ln\left(\frac{R_2}{R_1}\right)\frac{\cos\theta}{\sqrt{1-\sin^2\theta\sin^2\alpha_0}\sqrt{\cos^2\theta+\sin^2\theta\cos^2\alpha_0}}. \tag{A7}$$

If there is eccentric distance ΔR for I_{pri} as shown in Fig. 2(c), the equivalent integration area changes from $[R_1, R_2]$ to

$$\begin{aligned} z_1 &= R_1^2 + \Delta R^2 - 2R_1\Delta R\cos(\alpha_0) \\ z_2 &= R_2^2 + \Delta R^2 - 2R_2\Delta R\cos(\alpha_0) \end{aligned}. \tag{A8}$$

M can be derived as

$$M = h\int_{z_1}^{z_2}\frac{\mu_0}{2\pi r}dr = \frac{\mu_0 h}{4\pi}\ln\left(\frac{R_2^2+\Delta R^2-2R_2\Delta R\cos(\alpha_0)}{R_1^2+\Delta R^2-2R_1\Delta R\cos(\alpha_0)}\right). \tag{A9}$$

It can be seen that if there is an inclination angle and eccentric distance, M changes with the position of turn (i.e., α_0).

B. Derivation of Equivalent Impedance of Rogowski Coil

The transfer function of the Rogowski coil Z_{HF} is similar with transmission line, which has been well known as

$$Z_{\text{HF}} = \frac{j\omega M_0 R_L}{\gamma\left(Z_0 + R_L\coth(\gamma\alpha_l)\right)} \tag{A10}$$

where $Z_0 = \sqrt{Z_{\text{eq0}}/Y_{\text{eq0}}}$, and $\gamma = \sqrt{Z_{\text{eq0}}Y_{\text{eq0}}}$. Considering C_{tt0}, R_0 and M_0 can be ignored compared to L_{s0}, Z_0 and γ can be described by

$$Z_0 = \sqrt{L_{s0}/C_{tg0}}, \gamma = j\omega\sqrt{L_{s0}C_{tg0}} \tag{A11}$$

α_{l} represents the location of R_{L}, satisfying that

$$L_s = \alpha_l L_{s0},\ C_{tg} = \alpha_l C_{tg0}, M = \alpha_l M_0. \tag{A12}$$

Therefore, Z_{HF} can be represented as

$$Z_{HF} = \frac{j\omega M R_L}{j\omega L_s + \omega\sqrt{L_s C_{tg}}R_L\cot\left(\omega\sqrt{L_s C_{tg}}\right)}. \tag{A13}$$

With a relatively LF, $\omega\sqrt{L_s C_{tg}}$ is small, satisfying that

$$cot\left(\omega\sqrt{L_s C_{tg}}\right) \approx \frac{1}{\omega\sqrt{L_s C_{tg}}} \tag{A14}$$

Z_{HF} can be simplified as

$$Z_{\text{HF}} = \frac{j\omega M R_L}{j\omega L_s + R_L}. \tag{A15}$$

With a HF, $\omega\sqrt{L_s C_{tg}}$ could reach π, satisfying that

$$\cot\left(\omega\sqrt{L_s C_{tg}}\right) \to \infty \tag{A16}$$

It is easily obtained that $Z_{\text{HF}} = 0$ according to (A13).

C. Derivation of Signal Conditioning Circuit

As shown in Fig. 8, the output of the conditioning circuit V_{CS} satisfies that

$$\frac{V_{\text{CS}} - V_{\text{Rogo}}}{R_2/(1+j\omega R_2 C_1)} = \frac{V_{\text{Rogo}}}{R_1} + \frac{V_{\text{Rogo}} + V_{\text{TMR}}}{R_3}. \tag{A17}$$

In the case that R_1 is much smaller than R_2 and R_3, (A17) can be simplified as

$$V_{\text{CS}} = \frac{R_2(1+j\omega R_1 C_1)}{R_1(1+j\omega R_2 C_1)}V_{\text{Rogo}} + \frac{R_2/R_3}{1+j\omega R_2 C_1}V_{\text{TMR}}. \tag{A18}$$

Equations (12)–(16) in Section IV can be obtained accordingly.

ACKNOWLEDGMENT

The authors would like to thank for the support from the Tsinghua University (Department of Electrical Engineering) - China Southern Power Grid Technology Co., Ltd Joint Research Center for Power Electronics for Distributed Renewable Energy.

REFERENCES

[1] M. Nawaz, N. Chen, F. Chimento, and L. Wang, "Static and dynamic characterization of high power silicon carbide BJT modules," in *Proc. IEEE Energy Convers. Congr. Expo.*, 2014, pp. 2824–2831.

[2] Z. Zhang, B. Guo, F. Wang, E. Jones, L. Tolbert, and B. Blalock, "Methodology for wide band-gap device dynamic characterization," *IEEE Trans. Power Electron.*, vol. 32, no. 12, pp. 9307–9318, Dec. 2017.

[3] K. Ma, B. He, X. Xin, and X. Cai, "Capacitor voltage control for mission profile emulator of submodule in modular multilevel converter," *IEEE Trans. Power Electron.*, vol. 36, no. 11, pp. 12355–12364, Nov. 2021.

[4] M. Buffolo et al., "Review and outlook on GaN and SiC power devices: Industrial state-of-the-art, applications, and perspectives," *IEEE Trans. Electron Dev.*, vol. 71, no. 3, pp. 1344–1355, Mar. 2024.

[5] Z. Xin, H. Li, Q. Liu, and P. C. Loh, "A review of megahertz current sensors for megahertz power converters," *IEEE Trans. Power Electron.*, vol. 37, no. 6, pp. 6720–6738, Jun. 2022.
[6] CREE, "Silicon carbide power products datasheet," Nov. 2023. [Online]. Available: https://www.wolfspeed.com/products/power/sic-mosfets/
[7] K. Li, A. Videt, and N. Idir, "Using current surface probe to measure the current of the fast power semiconductors," *IEEE Trans. Power Electron.*, vol. 30, no. 6, pp. 2911–2917, Jun. 2015.
[8] G. Qiu, L. Ran, H. Feng, H. Jiang, H. Mao, and J. Wei, "A high-precision sensor based on AC flux cancellation for DC bias detection in dual active bridge converters," *IEEE Trans. Power Electron.*, vol. 37, no. 11, pp. 13513–13524, Nov. 2022.
[9] H. Wang, S. Ji, D. Mou, L. Yuan, Y. Zeng, and Z. Zhao, "Switching characterization and power loss optimization for modular multiactive bridge converter under common phase shift control," *IEEE J. Emerg. Sel. Topics Power Electron.*, vol. 11, no. 4, pp. 3924–3936, Aug. 2023.
[10] H. Wang, Y. Zeng, S. Ji, Z. Zhao, L. Yuan, and X. Mo, "ZVS soft switching operation region analysis of modular multi active bridge converter under single phase shift control," *IEEE Trans. Ind. Electron.*, vol. 70, no. 7, pp. 6865–6875, Jul. 2023.
[11] S. Ji, S. Zheng, F. Wang, and L. Tolbert, "Temperature-dependent characterization, modeling and switching speed limitation analysis of third generation 10 kV SiC MOSFET," *IEEE Trans. Power Electron.*, vol. 33, no. 5, pp. 4317–4327, May 2018.
[12] S. Ji, X. Huang, J. Palmer, F. Wang, and L. Tolbert, "Modular multilevel converter (MMC) modeling considering submodule voltage sensor noise," *IEEE Trans. Power Electron.*, vol. 36, no. 2, pp. 1215–1219, Feb. 2021.
[13] F. Lee, S. Wang, and L. Qiang, "Next generation of power supplies—Design for manufacturability," *IEEE J. Emerg. Sel. Topics Power Electron.*, vol. 9, no. 6, pp. 6462–6475, Dec. 2021.
[14] T&M Research Products Inc., "Series SDN/SSDN-414 datasheet," Jan. 2024. [Online]. Available: https://www.tandmresearch.com/uploads/images/Products/SDN_SDN-414_Short.PDF
[15] W. Zhang, Z. Zhang, F. Wang, E. Brush, and N. Forcier, "High-bandwidth low-inductance current shunt for wide-bandgap devices dynamic characterization," *IEEE Trans. Power Electron.*, vol. 36, no. 4, pp. 4522–4531, Apr. 2021.
[16] PEM, CWT Mini, "Current probe Datasheet," Feb. 2020. [Online]. Available: https://www.pemuk.com/Userfiles/CWTmini/CWT_Mini_DS_Feb_2020.pdf
[17] W. Zhang, S. Sohid, F. Wang, H. Cui, and B. Holzinger, "High-bandwidth combinational Rogowski coil for SiC MOSFET power module," *IEEE Trans. Power Electron.*, vol. 37, no. 4, pp. 4397–4405, Apr. 2022.
[18] ATO, "Current transformer catalog," Jan. 2024. [Online]. Available: https://www.ato.com/Content/doc/current-transformer-catalog.pdf
[19] N. Kondrath and K. Kazimierczuk, "Bandwidth of current transformers," *IEEE Trans. Instrum. Meas.*, vol. 58, no. 6, pp. 2008–2016, Jun. 2009.
[20] M. Fritsch and M. Wolter, "High-frequency current transformer design and construction guide," *IEEE Trans. Instrum. Meas.*, vol. 71, 2022, Art. no. 9004309.
[21] LEM, "Current transducer datasheet," Jul. 2015. [Online]. Available: https://www.lem.com/sites/default/files/products_datasheets/hal_50_600-s.pdf
[22] Tektronix, "TCP202 instruction manual," Jan. 2024. [Online]. Available: https://download.tek.com/manual/070954202.pdf
[23] M. Crescentini, M. Marchesi, A. Romani, M. Tartagni, and P. Traverso, "Bandwidth limits in hall effect-based current sensors," *ACTA IMEKO*, vol. 6, no. 4, pp. 17–24, Dec. 2017.
[24] S. Sanfilippo, "Hall probes: Physics and application to magnetometry," Mar. 2011, arXiv. [Online]. Available: https://arxiv.org/pdf/1103.1271
[25] J. Sanchez et al., "Electrical characterization of a magnetic tunnel junction current sensor for industrial applications," *IEEE Trans. Magn.*, vol. 48, no. 11, pp. 2823–2826, Nov. 2012.
[26] P. Li et al., "A contactless current sensor based on TMR chips," *IEEE Trans. Instrum. Meas.*, vol. 71, 2022, Art. no. 9511711.
[27] Y. Feng, S. Shao, J. Du, Q. Chen, J. Zhang, and X. Wu, "Short-circuit and over-current fault detection for SiC MOSFET modules based on tunnel magnetoresistance with predictive capabilities," *IEEE Trans. Power Electron.*, vol. 37, no. 4, pp. 3719–3723, Apr. 2022.
[28] Allegro Microsystems, "XtremeSense TMR current sensor datasheet," Feb. 2024. [Online]. Available: https://www.allegromicro.com/en/products/sense/current-sensor-ics/zero-to-fifty-amp-integrated-conductor-sensor-ics/CT433
[29] Aim-TTi, "I-prober 520 positional current probe," Jan. 2024. [Online]. Available: https://www.aimtti.com/go/iprober/index.php
[30] Iwatsu, "Optical probe electric current sensor: OpECS," Jan. 2024. [Online]. Available: https://www.iwatsu.com/tme/opecs/
[31] N. Karrer, P. Hofer-Noser, and D. Henrard, "HOKA: A new isolated current measuring principle and its features," in *Proc. IEEE IAS Annu. Meeting*, 1999, pp. 2121–2128.
[32] Z. Qi et al., "A high-bandwidth and easy-to-integrate parasitics-based switching current measurement method for fast GaN devices," *IEEE Trans. Power Electron.*, vol. 38, no. 1, pp. 447–459, Jan. 2023.
[33] J. Carrasco, E. Sanchis-Kilders, D. Ramirez, and E. J. Dede, "Improved magnetic coupled current sensing techniques," in *Proc. IEEE Power Electron. Specialists Conf.*, 1996, pp. 829–834.
[34] P. Poulichet, F. Costa, and E. Laboure, "A new high-current large-bandwidth DC active current probe for power electronics measurements," *IEEE Trans. Ind. Electron.*, vol. 52, no. 1, pp. 243–254, Feb. 2005.
[35] L. Dalessandro, N. Karrer, and J. W. Kolar, "High-performance planar isolated current sensor for power electronics applications," *IEEE Trans. Power Electron.*, vol. 22, no. 5, pp. 1682–1692, Sep. 2007.
[36] P. Niklaus, D. Bortis, and J. Kolar, "Beyond 50 MHz bandwidth extension of commercial DC-current measurement sensors with ultra-compact PCB-integrated pickup coils," *IEEE Trans. Ind. Appl.*, vol. 58, no. 4, pp. 5026–5041, Jul./Aug. 2022.
[37] T. Funk and B. Wicht, "A fully integrated DC to 75 MHz current sensing circuit with on-chip Rogowski coil," in *Proc. IEEE Custom Integr. Circuits Conf.*, 2018, pp. 1–4.
[38] J. Jiang and K. Makinwa, "11.3 A hybrid multipath CMOS magnetic sensor with 210μTrms resolution and 3 MHz bandwidth for contactless current sensing," in *Proc. IEEE Int. Solid-State Circuits Conf.*, 2016, pp. 204–205.
[39] S. J. Nibir, M. Biglarbegian, and B. Parkhideh, "A non-invasive DC-10-MHz wideband current sensor for ultra-fast current sensing in high-frequency power electronic converters," *IEEE Trans. Power Electron.*, vol. 34, no. 9, pp. 9095–9104, Sep. 2019.
[40] A. P. Sirat, H. Niakan, J. Gafford, and B. Parkhideh, "Design and development of hybrid current sensors for wide-bandgap power electronics applications," in *Proc. IEEE Appl. Power Electron. Conf. Expo.*, 2024, pp. 260–266.
[41] N. Tröster, J. Wölfle, J. Ruthardt, and J. Roth-Stielow, "High bandwidth current sensor with a low insertion inductance based on the HOKA principle," in *Proc. Eur. Conf. Power Electron. Appl.*, 2017, pp. 1–9.
[42] P. Ziegler, Y. Zhao, J. Haarer, J. Ruthardt, M. Fischer, and J. Roth-Stielow, "Compact design of a wide bandwidth high current sensor using tilted magnetic field sensors," *IEEE Trans. Ind. Appl.*, vol. 59, no. 6, pp. 7052–7060, Nov./Dec. 2023.
[43] M. Pozar, *Microwave Engineering*. Hoboken, NJ, USA: John Wiley & Sons, 2011.

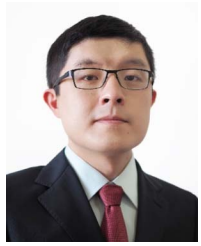

Shiqi Ji (Senior Member, IEEE) received the B.S. and Ph.D. degrees in electrical engineering from the Tsinghua University, Beijing, China, in 2010 and 2015, respectively.

Since 2015, he joined the Ultra-Wide Area Resilient Electric Energy Transmission Networks (CURENT), the University of Tennessee, Knoxville, TN, USA, and became a Research Assistant Professor in 2019. Since 2020, he has been with Tsinghua University, as an Assistant Professor, and then became an Associate Professor in 2021. He has authored or coauthored more than 80 technical papers in top journals and conference proceedings. His research interests include semiconductor device modeling, medium-voltage and high-power converter design, high-voltage SiC device characterization and application techniques, and grid-connected converter design.

Wenhao Xie (Student Member, IEEE) received the B.S. and M.E. degrees in electrical engineering from the Department of Electrical Engineering, Tsinghua University, Beijing, China, in 2021 and 2024, respectively.

His research interests include wide-band-gap semiconductors and application, geta driver, and advanced measurement technologies in power electronics.

Yikang Xiao (Student Member, IEEE) received the B.S. degree in electrical engineering in 2020 from the Department of Electrical Engineering, Tsinghua University, Beijing, China, where he is currently working toward the Ph.D. degree in electrical engineering.

His research interests include simulation of power electronics systems, modeling and characterization of power semiconductor devices, gate drive, and snubber circuit design for Si IGBTs and SiC MOSFETs.

Ran Lu is currently working toward the B.S. degree in electrical engineering with the Tsinghua University, Beijing, China.

His research interests include power electronics, particularly in relation to power semiconductor devices.

Zhengming Zhao (Fellow, IEEE) received the B.S. and M.S. degrees in electrical engineering from the Hunan University, Changsha, China, in 1982 and 1985, respectively, and the Ph.D. degree in electrical engineering from the Tsinghua University, Beijing, China, in 1991.

He is currently a Professor with the Department of Electrical Engineering, Tsinghua University. His research interests include high-power conversion, power electronics and motor control, and solar energy applications.

Chao Sheng received the B.S. and M.S. degrees in electrical engineering from the Tsinghua University, Beijing, China, in 1994 and 1997, respectively.

He is currently a Director with China Southern Power Grid Technology Company Ltd., Guangzhou, China. His current research interests include high-power conversion and power electronics.

Weitao Yang received the B.S. and Ph.D. degrees in materials science and engineering from the Zhejiang University, Hangzhou, China, in 2016 and 2021, respectively.

He is currently a Research Engineer with China Southern Power Grid Technology Company Ltd., Guangzhou, China. His current research interests include wide-bandgap semiconductor power devices and power electronic converters.